nature communications

Article

https://doi.org/10.1038/s41467-025-64140-4

Valence restrictive metal-support interaction for boosting catalytic activity of Rh/CeO_2 in CO_2 hydrogenation

Received: 21 March 2025

Accepted: 4 September 2025

Published online: 13 October 2025

Check for updates

Ze-Kai Yu[1,5], Mingxiang Jiang[2,5], Sheng Dai[3], Wangcheng Zhan[2] ✉, Zhi-Qiang Wang[1] ✉ & Xue-Qing Gong[4] ✉

Metal-support interactions (MSI) profoundly modulate the catalytic properties of supported nanometal catalysts. However, a comprehensive understanding of their underlying mechanisms largely remains elusive. In this work, we propose a novel valence restrictive metal-support interaction (VR-MSI) through systematic theoretical and experimental studies of the various Rh-modified CeO_2(111) surfaces. It reveals that small Rh clusters are oxidized by the CeO_2 support and constantly maintain the +2 valence state, thus establishing a clear correlation between their sizes and the electronic properties for each Rh atom. The VR-MSI effect can therefore favor the adsorptions of negatively charged species at small supported Rh clusters through local electrostatic interactions, and for CO_2 hydrogenation reactions, the occurrence of active hydride species (H^-) can be effectively promoted by the supported Rh nanocluster toward highly selective and active CO_2 hydrogenation to CH_4. This discovery broadens our understanding of the MSI effect and the mechanism of selective hydrogenation in heterogeneous catalysis, offering new insights into the rational design of advanced hydrogenation catalysts.

Metal-support interaction (MSI) plays a pivotal role in heterogeneous catalysis[1,2]. It profoundly influences the morphology and electronic structure of the metal catalyst, subsequently altering its stability and the catalytic activity and selectivity[1–7]. Previous studies have demonstrated that under reaction conditions, appropriate MSI can increase the catalytic reaction rate by nearly an order of magnitude[8]. To better understand the promotion effect of MSI, Campbell and co-workers proposed the idea of Electronic Metal-Support Interaction (EMSI), which suggests that the MSI can induce charge redistribution between the metal and oxide surfaces[9]. Lykhacht et al. and Chen et al. also demonstrated that EMSI can facilitate the electron transfer from the supported metal to the carrier, giving rise to the electronically modified metal and/or interfacial sites with higher activity[10,11].

As important active supports for metal catalysts that can offer unique MSI effects, the CeO_2 based materials have attracted significant attentions[3,12–16]. The CeO_2 carrier has been demonstrated to be capable of modulating the morphologies, electronic properties, and reactivities of the supported metal clusters/nanoparticles and promoting their effective stabilization and high dispersion[17–19]. Many metal/CeO_2 systems governed by MSI demonstrate excellent catalytic properties[20–22], among which the Rh/CeO_2 catalyst is particularly important[23–25]. Compared with other supported catalysts, such as Ni/

[1]State Key Laboratory of Green Chemical Engineering and Industrial Catalysis, Centre for Computational Chemistry and Research Institute of Industrial Catalysis, School of Chemistry and Molecular Engineering, East China University of Science and Technology, Shanghai, China. [2]State Key Laboratory of Green Chemical Engineering and Industrial Catalysis, Research Institute of Industrial Catalysis, School of Chemistry and Molecular Engineering, East China University of Science and Technology, Shanghai, China. [3]Key Laboratory for Advanced Materials, Feringa Nobel Prize Scientist Joint Research Center, School of Chemistry and Molecular Engineering, East China University of Science and Technology, Shanghai, China. [4]State Key Laboratory of Synergistic Chem-Bio Synthesis, School of Chemistry and Chemical Engineering, Shanghai Jiao Tong University, Shanghai, China. [5]These authors contributed equally: Ze-Kai Yu, Mingxiang Jiang. ✉e-mail: zhanwc@ecust.edu.cn; zhiqiangwang@ecust.edu.cn; xqgong@sjtu.edu.cn

CeO_2, Rh/CeO_2 not only exhibits superior reactivity, it also possesses greater resistance to sulfur poisoning and deactivation[26,27]. Notably, numerous studies have shown that altering the morphology of Rh/CeO_2 can significantly affect its catalytic activity, resulting in different selectivity for products such as CO, CH_4, HCOOH, or C_2H_5OH[24,25,28]. However, there still lacks a basic understanding of the electronic properties and their relationship with MSI for this system, and the potential mechanism of CO_2 hydrogenation on these catalysts also remains to be elucidated.

In this work, we first calculated the thermodynamic stabilities of various Rh-modified $CeO_2(111)$ surfaces under reaction conditions by plotting the computational phase diagrams. The results indicated that the supported Rh clusters are oxidized and maintained as Rh_n^{2+} by CeO_2, resulting in higher positive charge densities in the smaller Rh clusters. To leverage such valence-restrictive metal-support interaction (VR-MSI) effect, we prepared the Rh/CeO_2 catalysts with varying Rh sizes. The single-atom doped Rh catalyst (Rh_1-CeO_2) can preferentially catalyze the hydrogenation of CO_2 to CO, whereas those with supported Rh clusters favor CH_4 production. The combined theoretical and experimental results revealed that CO_2 on the Rh_1-CeO_2 selectively forms the COOH* intermediates via a dynamic hydrogenation mechanism, leading to the final product of CO, while the reaction on the supported Rh catalysts follows a direct hydrogenation mechanism, generating the HCOO* intermediates that lead to selective formation of CH_4. Interestingly, the unique VR-MSI effect of the catalyst with small Rh nanoclusters (Rh_{NC}/CeO_2) can help stabilize the key intermediates and improve the activity and selectivity of CO_2 hydrogenation to generate CH_4. This work reveals the close relationship between the electronic properties of the supported metal and the nature of key reaction intermediates in the Rh/CeO_2 catalyzed CO_2 hydrogenation, and how they may further determine the reactivity and product selectivity. It also shows that the VR-MSI can be an effective strategy for developing catalysts for CO_2 methanation, which may promote synthetic natural gas (SNG) production and "power-to-gas" application.

Results

Construction of Rh-modified $CeO_2(111)$ surfaces

We systematically investigated the stable structures of the different $CeO_2(111)$ surfaces modified by Rh under a reducing atmosphere using density functional theory (DFT) calculations and *p-T* phase diagrams. The calculated configurations included monatomic Rh oxide clusters with varying oxygen contents ($RhO_x/Ce_{48}O_{96}$, $x = 1 \sim 3$), single-atom Rh supported on the surface ($Rh_1/Ce_{48}O_{96}$), Rh clusters supported on the surface ($Rh_3/Ce_{48}O_{96}$), Rh-doped surface ($Rh_1Ce_{47}O_{96}$), and Rh-doped surfaces with an oxygen vacancy ($Rh_1Ce_{47}O_{95}$) (see Fig. 1a, Supplementary Note 1, Supplementary Fig. 1 and Supplementary Table 1). The results revealed that the Rh-doped $CeO_2(111)$ prefers to occur, and it can also readily form the oxygen vacancy beside the Rh dopant under usual conditions (Fig. 1b, c). As the reducing atmosphere pressure and temperature increase, the $CeO_2(111)$ surface with supported Rh clusters then becomes favorable (Fig. 1d). Therefore, we chose the single-atom Rh doped $CeO_2(111)$ with an O vacancy and the $CeO_2(111)$ with a supported Rh cluster in the subsequent study.

Valence restrictive metal-support interaction

Using the determined structures, we performed the electronic property calculations for the Rh-doped $CeO_2(111)$ surface with an oxygen vacancy ($Rh_1Ce_{47}O_{95}$, denoted as Rh_1-CeO_2) and the $CeO_2(111)$ surface with the supported Rh clusters with varying sizes (Rh_n/CeO_2). For the Rh_1-CeO_2 surface, the calculated spin charge density differences suggested that the two electrons brought by the oxygen vacancy are localized at both the Rh and Ce sites (Fig. 2a), resulting in the reduction of Rh^{4+} and Ce^{4+} to Rh^{3+} and Ce^{3+}, respectively (see the calculated Bader charges in Supplementary Fig. 3). In addition, the calculated density of states (DOS) revealed that the valence electron energy levels of the doped Rh are close to the populated Ce-4*f* states (Fig. 2a), indicating that the Rh^{3+} may exhibit similar electron-donating capacity as Ce^{3+}.

Regarding the $CeO_2(111)$ surfaces with supported Rh clusters, we focused on the $Rh_3/CeO_2(111)$ and $Rh_9/CeO_2(111)$ model systems. The calculated spin charge density differences indicated that in both systems, two Ce^{4+} cations take two electrons from the Rh clusters, resulting in their reduction to two Ce^{3+} species (Fig. 2a). As evidenced by our DOS calculations for Rh_3 and Rh_9 at $CeO_2(111)$ (Fig. 2a), the valence band maximum (VBM) is primarily contributed by Rh 4*d* states, indicating that Rh dictates the electron-donating capacity near the Fermi level. Moreover, the unoccupied Rh states in the conduction band also lie significantly below the empty Ce 4*f* states. This energy level alignment prevents further electron transfer from the partially oxidized Rh cluster to the Ce 4*f* states after the two-electron transfer. Our calculations also showed that other Rh_n clusters smaller than a critical size are consistently oxidized to the + 2 valence state (Supplementary Fig. 4), and we referred to this phenomenon as the valence-restricted metal-support interaction (VR-MSI) effect. For much larger Rh clusters, the VR-MSI effect becomes much less significant for the average atoms. For example, though the supported Rh_{22} forms Rh_{22}^{3+}, the positive charges of each Rh atoms are low enough to resemble a metallic state (Supplementary Figs. 4 and 5). Similar VR-MSI effects were also determined in our calculations for Ni, Pd, and Pt clusters on the $CeO_2(111)$ (Supplementary Fig. 6), but not in the system with anatase $TiO_2(101)$ as the support (Supplementary Fig. 7). These results highlight the pivotal role of the strongly localized Ce 4*f* states in driving this effect.

Further analysis revealed that VR-MSI is closely associated with local structural constraints at the $Rh/CeO_2(111)$ interface. For small Rh clusters stabilized in the + 2 valence state by VR-MSI, the relaxation of interfacial Ce and O atoms is moderate (Fig. 2b). The limited relaxation is crucial, as the reduction of Ce^{4+} to the bigger Ce^{3+} ions inherently induces localized strain, which then prevents the formation of excess Ce^{3+} ions near small Rh clusters or more electron transfer. On the other hand, as the Rh cluster size increases (like Rh_{22} and Rh_{31}, see Fig. 2b), the larger metal-support contact area can facilitate more pronounced interfacial relaxation, and such enhanced relaxation can more effectively accommodate a greater number of Ce^{3+} ions, allowing larger clusters to donate a greater total number of electrons to the support.

To elucidate the potential catalytic activities of the various Rh-modified CeO_2 surfaces, we first calculated the adsorptions of single H species on these surfaces. Two types of adsorbed H species were determined on the Rh_1-$CeO_2(111)$ surface: H at the Rh site (H_{Rh}, exothermic by 0.10 eV) and H at the oxygen vacancy (H_{Ov}, endothermic by 1.11 eV). The H_{Rh} species is negatively charged very slightly (Bader charge: − 0.07 |e| , Supplementary Fig. 8a). This could be due to the fact that the highly positive Rh^{3+} lacks the capacity to further transfer electron to the H species (Fig. 2c). In contrast, the H_{Ov} species carries a significant amount of negative charge (Bader charge: − 0.50 |e| , Supplementary Fig. 8b), forming ionic bonds with the neighboring Ce cations.

For the $Rh_n/CeO_2(111)$ surfaces, we calculated the H adsorptions at the hollow sites of the various Rh clusters ($n = 3 \sim 9$). The results showed that the smallest cluster, Rh_3, exhibits the highest activity for H adsorption (exothermic by 1.23 eV, Fig. 2c), and the adsorption strength decreased as the Rh cluster size increased, with the H adsorption energy on the Rh_9 cluster reaching 0.44 eV, nearly the same as that on the Rh surface (0.46 eV; see Fig. 2c and Supplementary Fig. 8). Bader charge calculations showed that the Rh_n clusters in the Rh_n/CeO_2 systems can transfer almost one extra electron to the adsorbed H (Supplementary Fig. 8). Interestingly, from the calculated electrostatic interaction energies (E_{EI}) between the $Rh^{\delta+}$ and H^- species in the series of $Rh_n/CeO_2(111)$ systems (Fig. 2d, Supplementary Table 2 and Supplementary Note 2), we can further learn that owing to the VR-

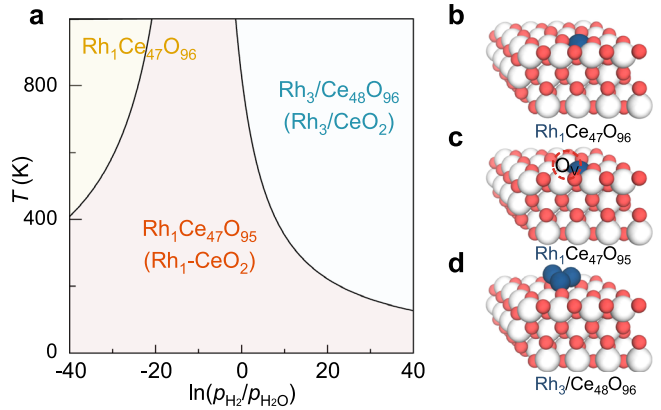

Fig. 1 | Stability analyses for Rh-modified CeO_2(111) surfaces. a calculated phase diagrams of Rh-modified CeO_2(111) under reducing atmosphere. **b**–**d** calculated structures of the Rh-doped CeO_2(111) surfaces ($Rh_1Ce_{47}O_{96}$) (**b**), the Rh-doped CeO_2(111) surface with an oxygen vacancy adjacent to the Rh site ($Rh_1Ce_{47}O_{95}$, also denoted as Rh_1-CeO_2) (**c**) and Rh cluster supported on the CeO_2(111) surface ($Rh_3/Ce_{48}O_{96}$, also denoted as Rh_3/CeO_2) (**d**). The dotted cycle in red represents the O vacancy. Red balls: O atoms; white balls: Ce atoms; navy blue balls: Rh atoms. This notation is used throughout the paper.

MSI effect in the Rh_n/CeO_2(111) system, the positive charge densities of the Rh species decrease with the increasing cluster size, and the electrostatic interactions between the adsorbed H^- and the neighboring Rh species also decrease accordingly, resulting in a decreasing H adsorption energy.

Catalytic CO_2 hydrogenation on Rh-modified CeO_2

Basing on the theoretical understandings of the size-dependent activities in the Rh/CeO_2 systems, we prepared a series of Rh-modified CeO_2 catalysts. Octahedral CeO_2 nanocrystals with exposed {111} facets were synthesized (Supplementary Fig. 9)[29], and Rh species were deposited under controlled temperatures (80 °C and 350 °C) and other conditions to obtain different types of Rh-modified CeO_2 catalysts, as guided by the thermodynamic phase diagram analysis (Fig. 1a). High-Angle Annular Dark Field Scanning Transmission Electron Microscopy (HAADF-STEM) and Energy Dispersive Spectroscopy (EDS) images showed that the catalyst prepared at 80 °C mainly contained atomically dispersed Rh species, designated as Rh_1-CeO_2 (Fig. 3a and Supplementary Fig. 10), and that synthesized at 350 °C mainly involved Rh nanoclusters, designated as Rh_{NC}/CeO_2 (Fig. 3b and Supplementary Fig. 10). Furthermore, the catalyst with high amount of Rh content on the CeO_2 was also prepared, for which the STEM analysis confirmed the presence of Rh nanoparticles with a diameter of ~ 3 nm, designated as Rh_{NP}/CeO_2 (Fig. 3c and Supplementary Figs. 10 and 11).

The local coordination environment of Rh was investigated by using the Fourier-transformed k^3-weighted extended X-ray absorption fine structure (EXAFS) in *R*-space (Fig. 3d, with the corresponding EXAFS fitting summarized in Supplementary Table 3 and Supplementary Fig. 12). The results revealed that the Rh_1-CeO_2 catalyst exhibited a single Rh-O coordination shell at ~ 1.5 Å (Fig. 3d, e), with a coordination number of 4.18 ± 0.45, indicating that the Rh species are doped as single atoms in the CeO_2 support[30], which is consistent with the calculated phase diagram. In contrast, the Rh_{NC}/CeO_2 and Rh_{NP}/CeO_2 catalysts gave a strong scattering peak at around 2.41 Å (Fig. 3d, f and g), corresponding to the Rh-Rh coordination shell. Among them, the Rh-Rh coordination number of the Rh_{NC}/CeO_2 catalyst is 1.68 ± 0.19, and the Rh-O coordination number is 3.47 ± 0.22[31], clearly indicating the formation of small Rh clusters. However, the Rh_{NP}/CeO_2 catalyst exhibited a high Rh-Rh coordination number (4.36 ± 0.35) and a low Rh-O coordination number (1.70 ± 0.38)[32], characteristic of supported metallic Rh nanoparticles. These results are also in line with the nanoparticle structures of the different Rh/CeO_2 catalysts observed by STEM.

The electronic properties of the Rh species were investigated by using in situ diffuse reflectance infrared Fourier transform spectroscopy of CO adsorption (in situ CO-DRIFTS), X-ray photoelectron spectroscopy (XPS), and normalized X-ray absorption near-edge structure (XANES). The Rh_1-CeO_2 catalyst exhibited the characteristic Rh^{3+} features in the CO-DRIFTS spectra, showing bands at 2110 and 2030 cm^{-1}, attributed to the symmetric and asymmetric vibrations of linearly adsorbed CO[23,32,33] (Fig. 3h). The absence of bridging CO bands further confirmed the atomic Rh dispersion, corroborated by the Rh^{3+} XPS peak at 308.9 eV[23,32] (Supplementary Fig. 13). For Rh_{NC}/CeO_2, besides the characteristic Rh^0 bands (2064 cm^{-1} for linear and 1858 cm^{-1} for bridge-bonded CO)[23,31], additional bands at 2094 and 2017 cm^{-1} were observed as well. Combined XPS analysis confirmed these features as CO adsorption at the $Rh^{\delta+}$ ($0 < \delta < 3$) sites[34]. Rh_{NP}/CeO_2 showed metallic Rh characteristics only, evidenced by the CO-DRIFTS bands at 2064 and 1858 cm^{-1} and the XPS peak at 307.4 eV[23,33](Supplementary Fig. 13). Normalized XANES results (Supplementary Fig. 14 and Supplementary Table 4) also established the order of Rh oxidation states as Rh_1-CeO_2 > Rh_{NC}/CeO_2 > Rh_{NP}/CeO_2, benchmarked against Rh foil and Rh_2O_3 standards[33,35]. The spectroscopic characterization results evidenced that the average oxidation state of Rh in the Rh_{NC}/CeO_2 systems maintains between Rh^{3+} and Rh^0. As the Rh nanoparticles occur, the VR-MSI effect on each Rh atom is then diminished, and it exhibits as the metallic one.

Next, we evaluated the catalytic performance of the three catalysts for CO_2 hydrogenation in the temperature range of 200 − 400 °C, where the reaction remains in the kinetically controlled region (see Supplementary Table 5). The determined activities followed the order Rh_{NC}/CeO_2 > Rh_{NP}/CeO_2 > Rh_1-CeO_2 (Fig. 3i), with the turnover frequencies (TOF) of 0.32, 0.23, and 0.20 s^{-1} at 290 °C, respectively. Notably, the TOF of Rh_{NC}/CeO_2 surpassed the previously reported similar catalysts under comparable conditions (Supplementary Table 6). Moreover, we also found that the CO_2 hydrogenation on the Rh_1-CeO_2 surface primarily produced CO, while both Rh_{NC}/CeO_2 and Rh_{NP}/CeO_2 favored the methane formation (Fig. 3j). In particular, Rh_{NC}/CeO_2 exhibited over 95% methane selectivity at temperatures above 250 °C, with a CH_4 yield significantly higher than that of Rh_{NP}/CeO_2 (23.7 mol_{CH4} $g_{Rh}^{-1}h^{-1}$ at 390 °C, see Supplementary Fig. 15). Moreover, the stability test of the Rh_{NC}/CeO_2 catalysts showed that the catalytic hydrogenation of CO_2 can maintain high conversion and selectivity at 300 and 400 °C for 75 h (Supplementary Fig. 16). Post-reaction XPS and STEM (Supplementary Figs 17 and 18) analyses also revealed that both the Rh_{NC}/CeO_2 and Rh_{NP}/CeO_2 catalysts kept their structural integrity and oxidation states.

Mechanistic study of CO_2 hydrogenation

To illustrate the relationship between the morphology and catalytic behavior of the supported Rh catalysts, we systematically calculated the CO_2 reduction pathways on the Rh_1-CeO_2(111), Rh_3/CeO_2(111), and Rh_9/CeO_2(111) model surfaces. The reaction generally involves CO_2 and H_2 adsorption, H_2 dissociation, and subsequent formation of different intermediates[36–40]. We considered three specific routes for CO_2 activation: (i) the direct dissociation of CO_2 to produce CO, (ii) the H^+/H^- species attacking the $C^{\delta+}$ of the adsorbed CO_2 to form the HCOO* intermediate, and (iii) the H^+/H^- species reacting with the $O^{\delta-}$ of the adsorbed CO_2 to form the COOH* species.

For Rh_1-CeO_2, the calculated results showed that CO_2 preferentially adsorbs at the Rh-O-Ce site, whereas H_2 prefers to adsorb at the Rh-O site (as detailed in Supplementary Note 3 and Supplementary Fig. 19). Moreover, the adsorption of CO_2 at the Rh-O-Ce site is much stronger than that of H_2 at the Rh-O site (1.66 eV *vs.* 0.56 eV, Supplementary Fig. 22), which suggests that CO_2 may compete with H_2 for the same adsorption sites. Under such conditions, the adsorbed H_2 may

https://doi.org/10.1038/s41467-025-64140-4

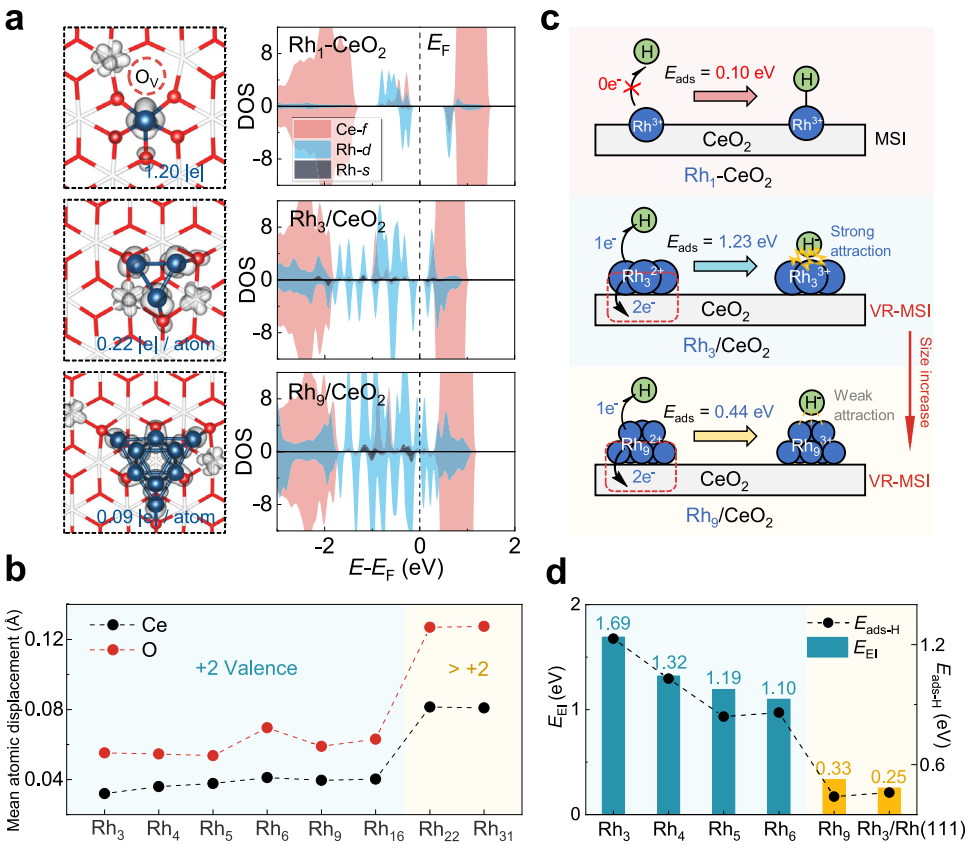

Fig. 2 | Illustration of valence restricted metal-support interaction (VR-MSI). **a** calculated spin charge density differences (gray) and density of states (DOS) of Rh_1-CeO_2(111), Rh_3/CeO_2(111) and Rh_9/CeO_2(111) surfaces. The average Bader charge per Rh atom is also shown. In the DOS plots, the red, blue, and black regions correspond to the projected Ce-*f*, Rh-*d*, and Rh-*s* orbitals, respectively. **b** mean atomic displacement of relaxed Ce and O atoms (top two O-Ce-O layers) on various Rh_n/CeO_2(111) surfaces (calculated with respect to unsupported CeO_2(111)). **c** schematic explanation of VR-MSI, the adsorption energy of H species and the electron transfer between H and Rh sites are also shown. **d** calculated the adsorption energy of H on the supported Rh clusters, as well as the electrostatic interaction energies (E_{EI}) between the H species and its three neighboring Rh atoms. Blue bars indicate smaller, more ionic Rh clusters, whereas yellow bars indicate more metallic Rh clusters.

undergo heterolytic dissociation at the oxygen vacancy site to produce one hydride and one proton species with the barriers of 0.77 eV (Fig. 4a). The calculations also showed that the direct dissociation of CO_2 into CO and O species is both thermodynamically and kinetically unfavorable (Fig. 4a). The process for the H^+/H^- species to attack the $C^{\delta+}$ of the adsorbed CO_2 to form HCOO* needs to overcome rather large barriers of 4.12/1.31 eV and is endothermic by 2.44/0.04 eV. However, H^+/H^- reaction with the $O^{\delta-}$ of the adsorbed CO_2 to form COOH* requires activation energies of 0.64/0.41 eV only and is exothermic by 0.20/1.45 eV. These results clearly suggested that during CO_2 hydrogenation, the H^+/H^- species can more readily react with the $O^{\delta-}$ of CO_2 than with the $C^{\delta+}$, leading to the preferential formation of COOH* and the subsequent production of CO. These results were confirmed by the in situ DRIFT spectra at 300 °C (see Supplementary Figs. 24 and 25, and consistent results were obtained at 250 °C, confirming mechanism robustness), which showed strong peaks of COOH* at 1680, 1622, and 1270 cm^{-1} and trivial ones of HCOO*[23,41,42]. It is noteworthy that although H^- species are more reactive than H^+ both kinetically and thermodynamically, kinetic studies on Rh_1-CeO_2 showed that at high H_2:CO_2 feed ratios, hydrogen spillover can occur, resulting in H^+ accumulation with high surface coverages and thus leading to comparable reactivity (Supplementary Note 4). In addition, our calculations also showed that when the H^- reacts with $O^{\delta-}$ of CO_2 to form COOH*, it actually turns to a H radical first by transferring one electron to the surface Ce^{4+} (Fig. 4b, c). One can therefore refer to such H species whose intrinsic properties change during the reaction as "dynamic hydrogen".

On the Rh_3/CeO_2(111) and Rh_9/CeO_2(111) surfaces, both CO_2 and H_2 preferentially adsorb on metallic Rh sites rather than at interfacial sites (as detailed in Supplementary Note 3 and Supplementary Figs. 20 and 22). The similar adsorption strengths of CO_2 and H_2 may lead to their co-adsorption, which would favor their subsequent reactions. Kinetic studies demonstrated that on both Rh_{NC}/CeO_2 and Rh_{NP}/CeO_2, the reaction orders of CO_2 and H_2 are similar, providing evidence for the co-adsorption mechanism (see Supplementary Note 4 and Supplementary Fig. 29). Notably, the adsorptions of CO_2 and H_2 are stronger at the supported Rh_3 than Rh_9, largely due to the stronger VR-MSI effect in the Rh_3/CeO_2 system. Our calculated results also showed that the homolytic H_2 dissociation for the generation of two H_{Rh} species can occur with the barriers of 0.04 and 0.02 eV only on the Rh_3/CeO_2(111) and Rh_9/CeO_2(111) surfaces, respectively (Fig. 4d). When the H_{Rh} species reacts with the $C^{\delta+}/O^{\delta-}$ of CO_2, it still stays at the surface site and retains the Rh-H bond in the transition state (Fig. 4e, f). Furthermore, the H_{Rh} reaction with the adsorbed CO_2 for HCOO* formation is kinetically and thermodynamically more favorable than COOH* formation on the Rh_n/CeO_2 surfaces (Fig. 4d). This can be attributed to the fact that the HCOO* species may interact with the surface more strongly through the bidentate O-Rh bonds, which also involve the favorable electrostatic attraction (Supplementary Table 7). In fact, since the smaller cluster Rh_3 has a stronger VR-MSI effect for each Rh atom, the local electrostatic attraction between Rh and HCOO* is further improved than that on the Rh_9 cluster, giving rise to its better stability (Supplementary Table 7). The in situ DRIFT spectra results (Supplementary Figs. 24 and 25) not only indicated the presence of

https://doi.org/10.1038/s41467-025-64140-4

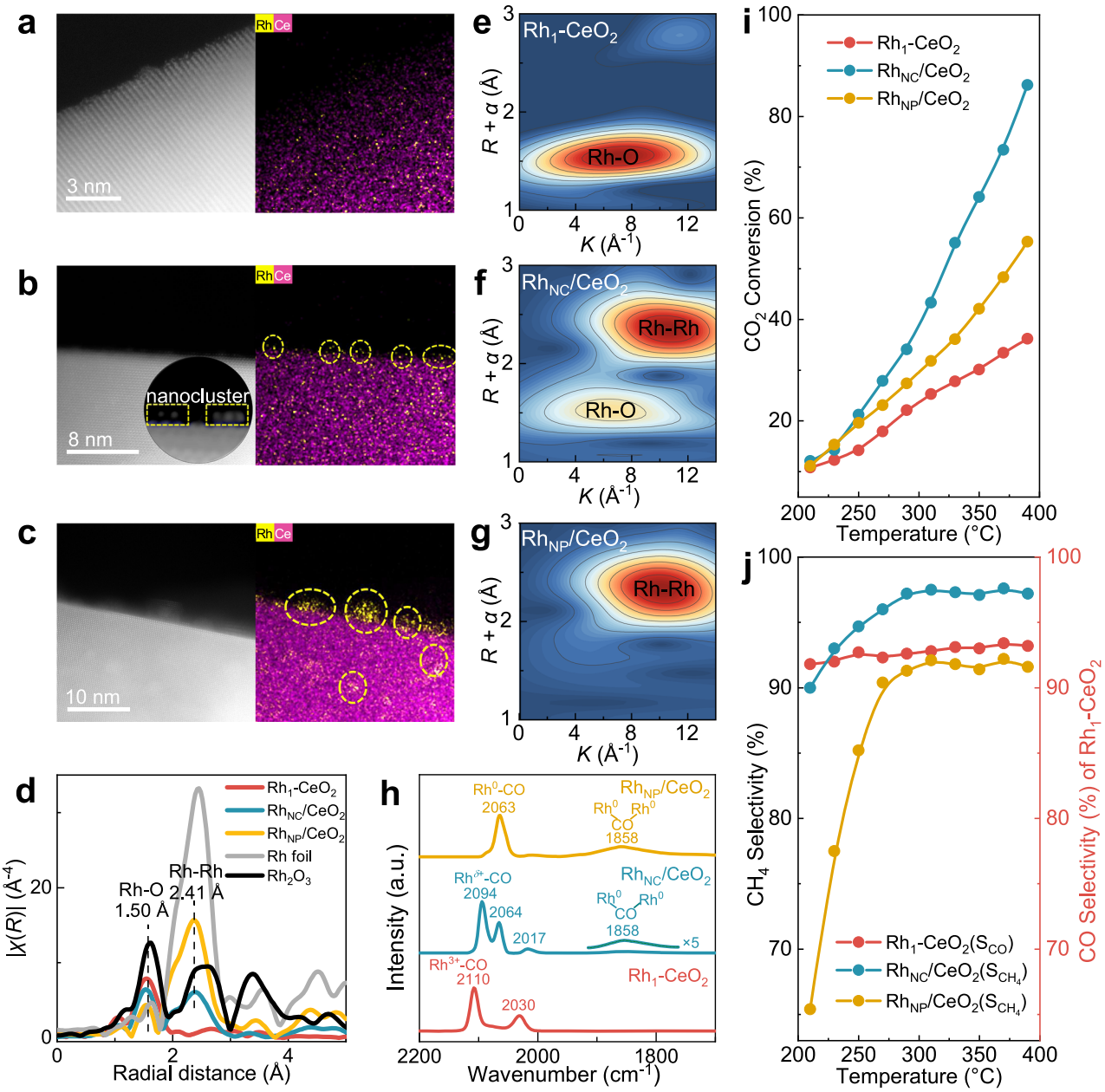

Fig. 3 | Experimental studies of the structures and catalytic hydrogenation activities of Rh/CeO_2. **a**–**c** high-angle annular dark field scanning transmission electron microscopy (HAADF-STEM, left) images and energy dispersive spectroscopy (EDS, right) elemental maps of Rh_1-CeO_2 (**a**), Rh_{NC}/CeO_2 (**b**), and Rh_{NP}/CeO_2 (**c**). EDS mapping: yellow = Rh, purple = Ce. The yellow dashed circle highlights the nanocluster in the STEM image and partial aggregated Rh structures in the EDS maps. **d** the Fourier transform of k^3-weighted extended X-ray absorption fine structure (EXAFS) spectra at the K-edge of Rh_1-CeO_2, Rh_{NC}/CeO_2, Rh_{NP}/CeO_2, Rh_2O_3, and Rh foil. **e**–**g** the wavelet transform analysis of Rh_1-CeO_2 (**e**), Rh_{NC}/CeO_2 (**f**) and Rh_{NP}/CeO_2 (**g**). **h** in situ CO-DRIFTS of Rh_1-CeO_2, Rh_{NC}/CeO_2, and Rh_{NP}/CeO_2, all labels denoted as "a.u." in this work represent "arbitrary units". **i**,**j** temperature-dependent CO_2 conversion (**i**) and product distribution (**j**) during CO_2 hydrogenation over various Rh/CeO_2 catalysts, where the red line on the right side of panel (**j**) represents the CO selectivity for the Rh_1-CeO_2 catalyst.

HCOO* (2962, 1550/1559, and 1384/1404 cm^{-1}) and they also showed the existence of the CH_3O* (2927 and 1469 cm^{-1}) species[42–44], clearly suggesting that the hydrogenation mechanism indeed follows the HCOO* pathway for the deep hydrogenation to CH_3O* and ultimately to CH_4.

Overall, the correlation between the Rh cluster size and the catalytic performance of the Rh-modified CeO_2 catalysts in CO_2 hydrogenation was explored and established. The enhanced catalytic activity and selectivity of small Rh clusters were attributed to the unique VR-MSI effect, which can improve the substrate adsorption and facilitate the formation of key intermediates.

Discussion

This study investigated the effect of interactions between metal and support on the catalytic activities of Rh-modified CeO_2 catalysts. The novel effect of valence-restricted metal-support interaction was proposed, which ensures the supported Rh clusters being consistently oxidized by CeO_2(111) to reach a general +2 state and corresponding more positive charges for each Rh atom in smaller clusters. Such a VR-MSI effect was verified by CO-DRIFTS, XPS, and XANES measurements. Theoretical calculations further showed that the small Rh cluster tuned by the VR-MSI effect can promote the adsorptions and occurrences of the negatively charged adsorbates,

https://doi.org/10.1038/s41467-025-64140-4

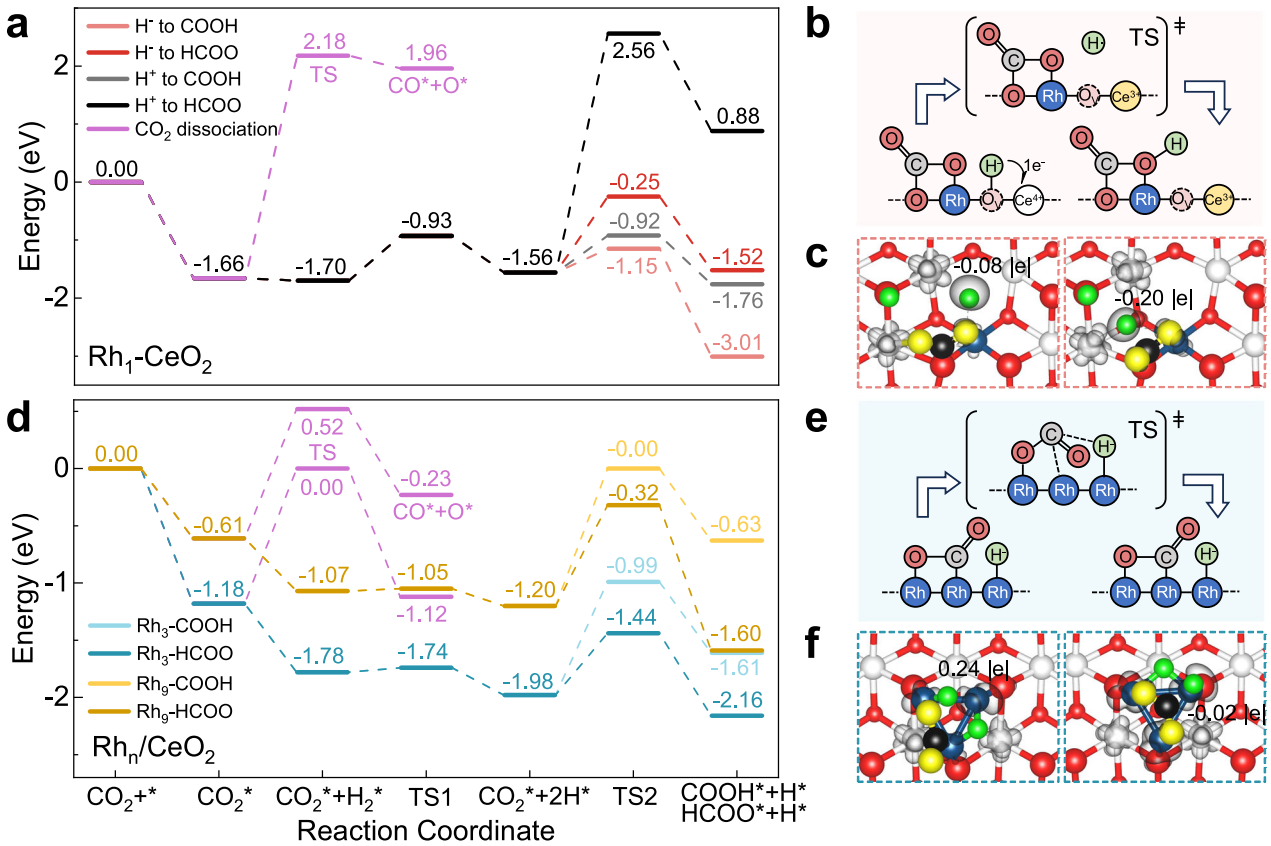

Fig. 4 | Theoretical simulation of CO_2 hydrogenation. a, **d** calculated energy profiles of CO_2 hydrogenation on the Rh_1-CeO_2(111) (**a**), Rh_3/CeO_2(111) and Rh_9/CeO_2(111) surfaces (**d**), with the corresponding structures provided in Supplementary Figs. 23, 26–28. **b**, **e** schematic illustration of the interaction of reactive H species with CO_2 on the Rh_1-CeO_2 (**b**) and Rh_3/CeO_2 surfaces (**e**). **c**, **f** calculated spin charge density differences (gray) of transition states of CO_2 hydrogenation on the Rh_1-CeO_2 (**c**) and Rh_3/CeO_2 surfaces (**f**) (left: transition state of the COOH* formation, right: transition state of the HCOO* formation). The Bader charges of the adsorbed hydrogen species are also shown. Black balls: C atoms; yellow balls: O atoms from CO_2.

including the hydride species, mainly through the favorable electrostatic interaction, which can be involved in the active and selective CO_2 hydrogenation to CH_4. The detailed reaction mechanisms were also determined through combined theoretical and experimental studies, and the nature of the differences in the selectivity and activity of the Rh-modified CeO_2 in catalytic CO_2 hydrogenation was shown to arise from the competitive formation of the HCOO* and COOH* intermediates. These results disclosed a new type of MSI effect exerted by the CeO_2 support through its unique 'quantized' 4*f* electron reservoir, which may help pave the way for the rational design of high-performance catalysts with tailored electronic properties and enhanced activities.

Methods

Computational methods

In this work, all spin-polarized DFT calculations were performed using the Vienna Ab-initio Simulation Package (VASP) version 5.4.4[45]. The projector augmented wave (PAW) method[46] and the Perdew-Burke-Ernzerhof (PBE) functional[47] under the generalized gradient approximation (GGA)[48] were applied. The kinetic energy cut-off was set to 400 eV, and the force threshold for structure optimizations was 0.05 eV/Å. By adopting these calculation settings, the optimized lattice parameter of CeO_2 (a = b = c = 5.456 Å) closely matches the experimental value (5.411 Å)[49], which was then used for the subsequent simulations.

For the model construction, a $p(4 \times 4)$ surface slab with three O-Ce-O atomic tri-layers was built for the CeO_2(111) surface. The top two tri-layers were allowed to fully relax, while the bottom one was kept fixed to mimic the bulk region. A large vacuum gap of 12 Å was used to eliminate the interaction between neighboring slabs, and the *k*-point mesh of $2 \times 2 \times 1$ suggested by previous studies was used for Brillouin-zone integrations[50]. Note that the on-site Coulomb interaction correction is necessary for accurately describing the localized Ce 4*f* electrons[51–53], and therefore we used an effective *U* value of 5 eV to describe the localized 4*f* orbitals of Ce.

The transition states (TSs) of surface reactions were located using a constrained optimization scheme and were verified when (i) all forces on the relaxed atoms vanish and (ii) the total energy is a maximum along the reaction coordination but a minimum with respect to the rest of the degrees of freedom[54–56].

The adsorption energy of species X on the surface, $E_{ads}(X)$, was calculated with

$$E_{ads}(X) = -(E_{X/slab} - E_{slab} - E_X) \quad (1)$$

where $E_{X/slab}$ is the calculated total energy of the adsorption system, while E_{slab} and E_X are the calculated energies of the clean surface and the gas phase molecule X, respectively. Accordingly, a positive $E_{ads}(X)$ value indicates an energetically favorable adsorption process, and the more positive the $E_{ads}(X)$ is, the more strongly the adsorbate X binds to the surface, and this definition was also proposed by Somorjai and Li[57].

The neutral oxygen vacancy formation energy (E_{Ov}) was calculated according to

$$E_{Ov} = E_{slab-vac} + 1/2E(O_2) - E_{slab} \quad (2)$$

where $E_{slab\text{-}vac}$ is the total energy of the surface with a neutral oxygen vacancy and $E(O_2)$ is the energy of a gas-phase O_2 molecule.

Catalyst preparation

The CeO_2 support with octahedral morphology was prepared by the hydrothermal method. Specifically, 2 mmol of $Ce(NO_3)_3{\cdot}6H_2O$ and 0.02 mmol of $Na_3PO_4{\cdot}12H_2O$ were dissolved in 80 mL of distilled water. After stirring at room temperature for 30 min, the solution was transferred to a Teflon-lined stainless-steel autoclave and heated at 170 °C for 10 h. The mixture was then cooled to room temperature and filtered to obtain the white solid. This solid was washed with distilled ethanol, dried at 120 °C for 12 h, and calcined in air at 400 °C for 4 h.

1 g of the as-prepared CeO_2 was mixed with 500 mL of deionized water, followed by ultrasonic dispersion for 20 min. Diluted nitric acid (HNO_3, pH ≈ 3) was added dropwise into the CeO_2 suspension under stirring, until the pH reached 3. Rhodium nitrate solution (0.1 g, 10.47 wt%) was prepared by dissolving rhodium nitrate ($Rh(NO_3)_3$) in deionized water and adjusting pH to 3 with HNO_3. This Rh solution was then added dropwise to the CeO_2 suspension, and the mixture was stirred for 4 h at room temperature, followed by filtration to obtain the solid. Finally, the solid was dried at 80 °C for 12 h, calcined in air at 450 °C for 4 h, and reduced in a flow of 10 vol% H_2 and 90 vol% Ar at 400 °C for 4 h. The obtained sample was named as Rh_{NP}/CeO_2.

In addition, we prepared 0.5-Rh_{NP}/CeO_2 by adding 0.05 g of rhodium solution (10.47 wt%) using the method described above. To synthesize the Rh/CeO_2 catalysts with different Rh particle sizes, including single atoms and clusters, the 0.5-Rh_{NP}/CeO_2 sample underwent hydrothermal redispersion followed by hydrogen treatment for aggregation. The sample was placed in a quartz glass tube and exposed to a flow of air containing 10 vol% H_2O (50 mL/min) at 750 °C for 25 h. After cooling to room temperature, the samples were dried in air at 80 °C for 12 h, resulting in the Rh/CeO_2 sample with single Rh atoms, named Rh_1-CeO_2. The Rh/CeO_2 sample with Rh clusters was synthesized using similar procedures, except that the sample was treated at 350 °C in a gas flow of 10 vol% H_2 and 90 vol% Ar for 12 h, and it was named Rh_{NC}/CeO_2.

Catalytic activity test

The catalytic performances of the catalyst for CO_2 hydrogenation were evaluated in a stainless steel fixed-bed reactor. Prior to the test, the catalyst was treated in a reducing atmosphere (10 vol% H_2 and 90 vol% Ar) at 200 °C for 1 h, and the effects of the treatment were confirmed by the H_2-Temperature Programmed Reduction (H_2-TPR) results (Supplementary Fig. 30). Then, 100 mg of catalyst was used, and the feed gas consisted of 19 vol% CO_2, 76 vol% H_2, and 5 vol% N_2 (H_2/CO_2 = 4:1) with a total gas hourly space velocity (GHSV) of 10000 mL·g^{-1}·h^{-1} at 0.1 MPa. The reaction was conducted over a temperature range of 200 ~ 400 °C and was maintained at a certain temperature for 30 min to achieve a steady state before testing. CO_2 conversion rate and the selectivity were measured using an online gas chromatograph (GC-2060) equipped with a flame ionization detector.

The formula for calculating the conversion rate of CO_2 is as follows:

$$X = \frac{n_{in} - n_{out}}{n_{in}} \times 100\% \quad (3)$$

where the n_{in} and n_{out} are the moles of CO_2 in the feed gas and exhaust gas, respectively.

The calculation for the turnover frequency (TOF) of the catalyst is as follows:

$$TOF = \frac{V_{CO_2} \cdot X_{CO_2} \cdot M_{Rh}}{m_{Rh} \cdot D_{Rh}} \quad (4)$$

Among them, X_{CO_2} is the conversion rate of CO_2, V_{CO_2} is the flow rate of CO_2 (mol/s), m_{Rh} is the mass of Rh in the tested catalyst (g), and M_{Rh} is the molar atomic mass of Rh (102.9055 g/mol); D_{Rh} is the dispersion of Rh and the dispersion of Rh_1-CeO_2 and Rh_{NC}/CeO_2 sample was set to 1, since our characterization confirmed that these Rh species exist either as isolated single atoms or as fully exposed few-atom monolayer clusters (Figs. 3a, b, e and f). For the Rh_{NP}/CeO_2 catalyst, the Rh dispersion was determined by CO pulse chemisorption, using a Micromeritics AutoChem II 2920 analyzer with an HPR-20 QIC mass spectrometer. A 30 mg catalyst sample was pretreated with 5% H_2/Ar at 300 °C for 30 min, cooled to 30 °C, and then exposed to 1% CO/He pulses (5 mL/min) every two minutes until a constant CO signal was obtained. The Rh dispersion was then calculated from the CO uptake, assuming a 1:1 CO-to-Rh active site ratio. For TOF measurements, the catalyst mass was reduced to 20 mg to maintain the conversions below 15%, ensuring differential reactor conditions and thus providing a more accurate assessment of the intrinsic turnover frequency.

The selectivity for CO or CH_4 formation in CO_2 hydrogenation was calculated as follows:

$$Selectivity_{CO\,or\,CH_4} = \frac{n_{CO\,or\,CH_4}}{(n_{CO} + n_{CH_4})} \quad (5)$$

Among them, the n_{CO} and n_{CH_4} are the moles of CO and CH_4 in the exhaust gas, respectively.

Characterizations

Rh K-edge analysis was performed with Si(311) crystal monochromators at the BL14W1 beamlines at the Shanghai Synchrotron Radiation Facility (SSRF) (Shanghai, China). The Rh K-edge extended X-ray absorption fine structure (EXAFS) spectrum was recorded in transmission mode.

Aberration-corrected scanning transmission electron microscopy (AC-STEM) characterization was conducted on a Thermo Fisher Themis Z transmission electron microscope equipped with two aberration correctors. High-angle annular dark-field STEM images were captured using a convergence semi-angle of 25 mrad and inner and outer collection angles of 47 and 200 mrad, respectively. Energy dispersive X-ray spectroscopy (EDS) was carried out using four in-column Super-X detectors.

X-ray photoelectron spectroscopy (XPS) measurements were performed on a PHI-Quantera spectrometer with an Al anode (Al Kα = 1486.6 eV). Binding energy calibration was obtained using the C1*s* peak at 284.4 eV. Before XPS measurement, the sample was pre-treated with 10% H_2/Ar reduction at 310 °C for 1 h.

In situ diffuse reflectance infrared Fourier transform (DRIFT) spectra of CO adsorption on the catalyst were recorded on a Nicolet Nexus 670 Fourier transform infrared spectrometer, with 64 scans and an effective resolution of 4 cm^{-1}. The catalyst was first reduced in 10 vol % H_2 balanced with Ar at 300 °C for 1 h and purged by Ar at 150 °C for 30 min. After cooling to room temperature in Ar, a background spectrum was collected. The sample was then exposed to 10 vol% CO in Ar (20 mL/min^{-1}) for 30 min until CO adsorption saturation. Subsequently, the sample was purged with Ar (20 mL/min^{-1}) for another 30 min to remove the gas-phase CO, and the DRIFT spectrum was collected with 64 scans at a resolution of 4 cm^{-1}.

In situ DRIFT spectra of CO_2 hydrogenation were also recorded on the Nicolet Nexus 670 Fourier transform infrared spectrometer.

Before measurement, the sample was pre-treated in Ar at 300 °C for 1 h, and the background spectrum was recorded. A mixture of 19 vol% CO_2, 76 vol% H_2, and 5 vol% N_2 (50 mL/min) was then introduced, and the in situ DRIFTS spectra were collected over a specified period.

The contents of rhodium (Supplementary Table 8) were determined by inductively coupled plasma optical emission spectrometry (ICP-OES) using an Agilent (US) 5800 ICP-OES apparatus.

Data availability

Data are available from the corresponding authors upon request. Some of the data are also provided in the Supplementary Information and the Source Data file. Source data are provided in this paper.

References

1. Ro, I., Resasco, J. & Christopher, P. Approaches for understanding and controlling interfacial effects in oxide-supported metal catalysts. *ACS Catal.* **8**, 7368–7387 (2018).
2. Ahmadi, M., Mistry, H. & Roldan Cuenya, B. Tailoring the catalytic properties of metal nanoparticles via support interactions. *J. Phys. Chem. Lett.* **7**, 3519–3533 (2016).
3. Farmer, J. A. & Campbell, C. T. Ceria maintains smaller metal catalyst particles by strong metal-support bonding. *Science* **329**, 933–936 (2010).
4. Tauster, S. J., Fung, S. C., Baker, R. T. K. & Horsley, J. A. Strong interactions in supported-metal catalysts. *Science* **211**, 1121–1125 (1981).
5. Liu, X. et al. Strong metal-support interactions between gold nanoparticles and ZnO nanorods in CO oxidation. *J. Am. Chem. Soc.* **134**, 10251–10258 (2012).
6. Zhang, J., Zhu, D., Yan, J. & Wang, C.-A. Strong metal-support interactions induced by an ultrafast laser. *Nat. Commun.* **12**, 6665 (2021).
7. Tauster, S. J., Fung, S. C. & Garten, R. L. Strong metal-support interactions. Group 8 noble metals supported on titanium dioxide. *J. Am. Chem. Soc.* **100**, 170–175 (1978).
8. van Deelen, T. W., Hernández Mejía, C. & de Jong, K. P. Control of metal-support interactions in heterogeneous catalysts to enhance activity and selectivity. *Nat. Catal.* **2**, 955–970 (2019).
9. Campbell, C. T. Electronic perturbations. *Nat. Chem.* **4**, 597–598 (2012).
10. Lykhach, Y. et al. Counting electrons on supported nanoparticles. *Nat. Mater.* **15**, 284–288 (2016).
11. Chen, A. et al. Structure of the catalytically active copper-ceria interfacial perimeter. *Nat. Catal.* **2**, 334–341 (2019).
12. Parastaev, A. et al. Boosting CO_2 hydrogenation via size-dependent metal-support interactions in cobalt/ceria-based catalysts. *Nat. Catal.* **3**, 526–533 (2020).
13. Jiang, P. et al. Tuning oxidant and antioxidant activities of ceria by anchoring copper single-site for antibacterial application. *Nat. Commun.* **15**, 1010 (2024).
14. Xu, A. et al. Edge-rich Pt-O-Ce sites in CeO_2 supported patchy atomic-layer Pt enable a non-CO pathway for efficient methanol oxidation. *Angew. Chem. Int. Ed.* e202410545 (2024).
15. Gangarajula, Y. et al. Operando induced strong metal-support interaction of Rh/CeO_2 catalyst in dry reforming of methane. *Appl. Catal. B Environ.* **343**, 123503 (2024).
16. Zhan, P. et al. Efficient electrosynthesis of urea over single-atom alloy with electronic metal support interaction. *Angew. Chem. Int. Ed.* **63**, e202409019 (2024).
17. Pacchioni, G. & Freund, H.-J. Controlling the charge state of supported nanoparticles in catalysis: lessons from model systems. *Chem. Soc. Rev.* **47**, 8474–8502 (2018).
18. Zhou, Y. et al. Suppressing metal-support interaction enhances photothermal CO_2 methanation on the Ru/CeO_2 catalysts. *ACS Catal.* **14**, 14285–14296 (2024).
19. Yan, G. et al. Reaction product-driven restructuring and assisted stabilization of a highly dispersed Rh-on-ceria catalyst. *Nat. Catal.* **5**, 119–127 (2022).
20. Guo, Y. et al. Low-temperature CO_2 methanation over CeO_2-supported Ru single atoms, nanoclusters, and nanoparticles competitively tuned by strong metal-support interactions and H-spillover effect. *ACS Catal.* **8**, 6203–6215 (2018).
21. An, Z. et al. Shape dependency of CO_2 hydrogenation on ceria supported singly dispersed Ru catalysts. *J. Catal.* **429**, 115245 (2024).
22. Martin, N. M. et al. Structure-function relationship for CO_2 methanation over ceria supported Rh and Ni catalysts under atmospheric pressure conditions. *Catal. Sci. Technol.* **9**, 1644–1653 (2019).
23. Wu, D. et al. Nature and dynamic evolution of Rh single atoms trapped by CeO_2 in CO hydrogenation. *ACS Catal.* **12**, 12253–12267 (2022).
24. Liao, W. et al. Decoupling the interfacial catalysis of CeO_2-supported Rh catalysts tuned by CeO_2 morphology and Rh particle size in CO_2 Hydrogenation. *ACS Catal.* **13**, 5767–5779 (2023).
25. Zheng, K. et al. Ti-doped CeO_2 stabilized single-atom rhodium catalyst for selective and stable CO_2 hydrogenation to ethanol. *Angew. Chem. Int. Ed.* **61**, e202210991 (2022).
26. Struis, R. P. W. J. et al. Sulphur poisoning of Ni catalysts in the SNG production from biomass: A TPO/XPS/XAS study. *Appl. Catal. A Gen.* **362**, 121–128 (2009).
27. Ocsachoque, M. A., Eugenio Russman, J. I., Irigoyen, B., Gazzoli, D. & González, M. G. Experimental and theoretical study about sulfur deactivation of Ni/CeO_2 and Rh/CeO_2 catalysts. *Mater. Chem. Phy.* **172**, 69–76 (2016).
28. Wu, B., Yu, X., Huang, M., Zhong, L. & Sun, Y. Rh single atoms embedded in CeO_2 nanostructure boost CO_2 hydrogenation to HCOOH. *Chin. J. Chem. Eng.* **43**, 62–69 (2022).
29. Wang, Z. et al. Ru/CeO_2 catalyst with optimized CeO_2 support morphology and surface facets for propane combustion. *Environ. Sci. Technol.* **53**, 5349–5358 (2019).
30. Zheng, Y. et al. Boosting the hydroformylation activity of a Rh/CeO_2 single-atom catalyst by tuning surface deficiencies. *ACS Catal.* **13**, 7243–7255 (2023).
31. Jeong, H. et al. Fully dispersed Rh ensemble catalyst to enhance low-temperature activity. *J. Am. Chem. Soc.* **140**, 9558–9565 (2018).
32. Hülsey, M. J. et al. In situ spectroscopy-guided engineering of rhodium single-atom catalysts for CO oxidation. *Nat. Commun.* **10**, 1330 (2019).
33. Luo, L., Timoshenko, J., Lapp, A. S., Frenkel, A. I. & Crooks, R. M. Structural characterization of Rh and RhAu dendrimer-encapsulated nanoparticles. *Langmuir* **33**, 12434–12442 (2017).
34. Xie, S., Kim, D., Ye, K., Tetard, L. & Liu, F. Regulating local coordination environment of rhodium single atoms in Rh/CeO_2 catalysts for N_2O decomposition. *J. Rare Earth.* **41**, 941–951 (2023).
35. Asakura, H. et al. Dynamic behavior of Rh species in Rh/Al_2O_3 model catalyst during three-way catalytic reaction: an operando X-ray absorption spectroscopy study. *J. Am. Chem. Soc.* **140**, 176–184 (2017).
36. Wang, F., Wei, M., Evans, D. G. & Duan, X. CeO_2-based heterogeneous catalysts toward catalytic conversion of CO_2. *J. Mater. Chem. A* **4**, 5773–5783 (2016).
37. Wang, Z.-Q., Chu, D.-R., Zhou, H., Wu, X.-P. & Gong, X.-Q. Role of low-coordinated Ce in hydride formation and selective hydrogenation reactions on CeO_2 surfaces. *ACS Catal.* **12**, 624–632 (2022).
38. Zheng, H. et al. Unveiling the key factors in determining the activity and selectivity of CO_2 hydrogenation over Ni/CeO_2 catalysts. *ACS Catal.* **12**, 15451–15462 (2022).

39. Tang, Q. et al. Lattice-hydride mechanism in electrocatalytic CO_2 reduction by structurally precise copper-hydride nanoclusters. *J. Am. Chem. Soc.* **139**, 9728–9736 (2017).
40. Zhu, Y. et al. Environment of metal-O-Fe bonds enabling high activity in CO_2 reduction on single metal atoms and on supported nanoparticles. *J. Am. Chem. Soc.* **143**, 5540–5549 (2021).
41. Li, S. et al. Tuning the CO_2 hydrogenation selectivity of rhodium single-atom catalysts on zirconium dioxide with alkali ions. *Angew. Chem. Int. Ed.* **62**, e202218167 (2023).
42. Kattel, S., Liu, P. & Chen, J. G. Tuning selectivity of CO_2 hydrogenation reactions at the metal/oxide interface. *J. Am. Chem. Soc.* **139**, 9739–9754 (2017).
43. Yang, M. et al. Unlocking a dual-channel pathway in CO_2 hydrogenation to methanol over single-site zirconium on amorphous silica. *Angew. Chem. Int. Ed.* **63**, e202312292 (2023).
44. Wang, W., Qu, Z., Song, L. & Fu, Q. An investigation of Zr/Ce ratio influencing the catalytic performance of CuO/Ce_1-ZrO_2 catalyst for CO_2 hydrogenation to CH_3OH. *J. Energy Chem.* **47**, 18–28 (2020).
45. Kresse, G. & Furthmüller, J. Efficient iterative schemes for ab initio total-energy calculations using a plane-wave basis set. *Phys. Rev. B* **54**, 11169–11186 (1996).
46. Blochl, P. E. Projector augmented-wave method. *Phys. Rev. B* **50**, 17953–17979 (1994).
47. John, P. P. et al. M. Generalized gradient approximation made simple. *Phys. Rev. Lett.* **77**, 3865 (1996).
48. Teter, M. P., Payne, M. C. & Allan, D. C. Solution of Schrödinger's equation for large systems. *Phys. Rev. B* **40**, 12255–12263 (1989).
49. Kümmerle, E. & Heger, G. The structures of C-$Ce_2O_{3+\delta}$, Ce_7O_{12}, and $Ce_{11}O_{20}$. *J. Solid State Chem.* **147**, 485–500 (1999).
50. Jerratsch, J. F. et al. Electron localization in defective ceria films: a study with scanning-tunneling microscopy and density-functional theory. *Phys. Rev. Lett.* **106**, 246801 (2011).
51. Nolan, M., Grigoleit, S., Sayle, D. C., Parker, S. C. & Watson, G. W. Density functional theory studies of the structure and electronic structure of pure and defective low index surfaces of ceria. *Surf. Sci.* **576**, 217–229 (2005).
52. Nolan, M., Parker, S. C. & Watson, G. W. The electronic structure of oxygen vacancy defects at the low index surfaces of ceria. *Surf. Sci.* **595**, 223–232 (2005).
53. Vicario, G., Balducci, G., Fabris, S., Gironcoli, S. D. & Baroni, S. Interaction of hydrogen with cerium oxide surfaces: a quantum mechanical computational study. *J. Phys. Chem. B* **110**, 19380–19385 (2006).
54. Michaelides, A. et al. Identification of general linear relationships between activation energies and enthalpy changes for dissociation reactions at surfaces. *J. Am. Chem. Soc.* **125**, 3704–3705 (2003).
55. Alavi, A., Hu, P., Deutsch, T., Silvestrelli, P. L. & Hutter, J. CO oxidation on Pt(111): An ab initio density functional theory study. *Phys. Rev. Lett.* **80**, 3650 (1998).
56. Liu, Z. P. & Hu, P. General rules for predicting where a catalytic reaction should occur on metal surfaces: A density functional theory study of C-H and C-O bond breaking/making on flat, stepped, and kinked metal surfaces. *J. Am. Chem. Soc.* **125**, 1958–1967 (2003).
57. Somorjai, G. A. & Li, Y. *Introduction to Surface Chemistry and Catalysis*, 2nd Edition. (Wiley-VCH, Berkeley, CA, USA; 2010).

Acknowledgements

This work was supported by the National Key R&D Program of China (2023YFA1508500, 2021YFA1500700) and the National Natural Science Foundation of China (22203030).

Author contributions

Z.-K.Y. performed the DFT calculations, collected and analyzed the DFT data. M.X.J. performed materials synthesis, characterization, and performance experiments. S.D. performed the STEM experiments and the corresponding analysis. W.-C.Z. designed the experiments, analyzed the experiments data. Z.-Q.W. supervised the research, analyzed the DFT and experiments data and provided constructive suggestions. X.-Q.G. conceived the ideas, supervised the research and designed the present work. All authors contributed to the discussion and the manuscript writing.

Competing interests

The authors declare no competing interests.

Additional information

Supplementary information The online version contains supplementary material available at https://doi.org/10.1038/s41467-025-64140-4.

Correspondence and requests for materials should be addressed to Wangcheng Zhan, Zhi-Qiang Wang or Xue-Qing Gong.

Peer review information *Nature Communications* thanks Juan González-Velasco, and the other anonymous reviewer(s) for their contribution to the peer review of this work. A peer review file is available.